Oxygen-pressure Driven Balancing of Interface and Bulk Scattering in Amorphous Oxide Semiconductor Thin-Film Transistors

Che-Yi Lin[*,‡], Yu-Ching Kuo[‡], Yi-Chen Liu, Feng-Shou Yang, Yuan-Ming Chang, Po-Wen Chiu, Toshihide Nabatame, Mengjiao Li[*], Kazuhito Tsukagoshi[*] and Yen-Fu Lin[*]

Dr. C. Y. Lin, Y. C. Kuo, Y. C. Liu, Dr. F. S. Yang, Dr. Y. M. Chang, Prof. Y. F. Lin
Department of Physics, National Chung Hsing University, Taichung City, 40227, Taiwan
E-mail: joe801105@gmai.com; yenfulin@nchu.edu.tw

Dr. F. S. Yang, Prof. P. W. Chiu
Department of Electrical Engineering and Institute of Electronic Engineering, National Tsing Hua University, Hsinchu 300, Taiwan

Prof. M. Li
School of Microelectronics, Intelligent sensing chip technology Collaborative Innovation Center, Shanghai University, Jiading, Shanghai 201800, China
E-mail: mjli@shu.edu.cn

Dr. T. Nabatame, Dr. K. Tsukagoshi
Research Center for Materials Nanoarchitectonics (MANA), National Institute for Materials Science (NIMS), 1-1 Tsukuba, Ibaraki 305-0044, Japan
E-mail: TSUKAGOSHI.Kazuhito@nims.go.jp

‡C. Y. Lin and Y. C. Kuo contributed equally to this work.

Keywords: metal oxide semiconductor, thin-film transistors, Low-frequency noise, oxygen pressure, charge transport mechanism

Abstract

Oxygen vacancies (V_O) critically influence the electronic properties and stability of amorphous oxide semiconductor (AOS) thin-film transistors (TFTs). Here, we investigate the impact of oxygen partial pressure during film deposition on charge transport mechanisms in 10-nm-thick silicon-doped indium oxide (ISO) TFTs. By adjusting the Ar:O_2 ratio (11:1, 8:4, and 6:6), we observe a shift from interface-limited to bulk-scattering-dominated transport. Higher O_2 pressure leads to increased subthreshold swing (SS), positive threshold voltage (V_{th}) shifts, and larger current fluctuations, suggesting greater charge trapping and mobility degradation. Low-frequency noise (LFN) analysis further reveals a shift in the dominant noise mechanism: interface charge trapping dominates at low O_2 pressure, while bulk carrier scattering prevails at high O_2 pressure. The extracted trap density (N_{it}) increases by nearly two orders of magnitude, confirming the role of fully oxidized indium atoms in the conducting channel as charge-scattering centers. These findings establish oxygen pressure as a key parameter for balancing interface and bulk effects in AOS TFTs and provide a pathway for optimizing device performance and stability in next-generation oxide electronics.

1. Introduction

Oxygen vacancies (V_O) play a pivotal role in shaping the electronic properties and stability of oxide-based semiconductor devices.[1-10] As intrinsic defects, V_O not only influences carrier concentration by acting as electron donors but also impacts material conductivity, optical transparency, and long-term device performance. Their presence is essential for enabling conduction in oxide semiconductors, yet excessive V_O can lead to undesirable effects such as threshold voltage (V_{th}) shifts, current leakage, and reduced environmental stability.[11-16] This dual nature of oxygen vacancies highlights their critical importance in designing and optimizing oxide-based electronic devices, particularly thin-film transistors (TFTs), where the balance between sufficient carrier generation and device stability is crucial.[15]

In the context of amorphous oxide semiconductors (AOS), V_O become even more significant due to their unique electronic structure. Unlike covalent semiconductors, AOSs rely on the overlap of isotropic s-orbitals of heavy metal cations to achieve high electron mobility, even in amorphous states.[15] However, the presence of V_O introduces complexities such as environmental sensitivity, hysteresis, and instability under prolonged bias stress. These issues are particularly pronounced in indium gallium zinc oxide (a-IGZO) TFTs,[17] where excessive V_O formation has been linked to degradation mechanisms like negative bias stress and negative bias illumination stress.[13, 18-20] As understanding of V_O deepens, material engineering strategies such as dopant incorporation have emerged as effective tools to regulate V_O behavior. Dopants like tin (Sn), tungsten (W), titanium (Ti), scandium (Sc), boron (B), and silicon (Si), with strong oxygen bonding energy, significantly suppress excessive V_O and stabilize the surrounding oxide matrix, paving the way for enhanced device stability and performance.[21-30] These

insights underline the importance of controlling V_O as a critical step toward advancing oxide-based semiconductor technologies for next-generation TFTs and other applications.

Direct current (DC) measurements are a widely adopted method for investigating the electrical properties of AOS TFTs. However, their static nature limits their ability to capture the dynamic behavior of defect states, which critically influence carrier transport, recombination, and trapping, causing threshold voltage shifts and mobility changes. Low-frequency noise (LFN) measurements complement DC methods by providing insights into microscopic transport mechanisms and defect dynamics.[31] Through noise spectra such as 1/*f* or generation-recombination (G-R) noise, LFN can identify defect states, quantify their densities, and analyze their interactions with carriers.[32-36] Therefore, it can effectively reveal the role of V_O in charge trapping and de-trapping, as well as their spatial and temporal distributions in the channel layer and/or at the device interface. LFN also excels at studying stability under stress conditions like bias stress and thermal cycling, detecting subtle defect changes and early degradation, and offering a predictive framework for device reliability. This approach is vital for elucidating V_O-induced instability and improving the performance of emerging materials.

To examine how oxygen vacancies affect the performance and stability of AOS TFTs, in this work, 10-nm-thick silicon-doped indium oxide (ISO) films (In_2O_3: SiO_2 = 90:10 by weight) were fabricated as a model. The strong oxygen bond dissociation energy and high Lewis acid strength of silicon provide a robust framework for studying V_O-mediated electronic behaviors under varying oxygen pressures. The O_2 partial pressure ratio (Ar:O_2= 11:1, 8:4, and 6:6) was systematically adjusted during ISO film growth to analyze its effect on TFT performance. Higher oxygen partial pressure degrades TFT performance, increasing hysteresis (ΔV_{bg}), subthreshold swing (SS), and reducing mobility (μ) and the on/off current ratio (I_{on}/I_{off}). Additionally, higher oxygen pressure

caused a positive V_{th} shift and more variability between devices, indicating increased charge noise fluctuations. To explore the underlying physical mechanisms of these dynamic conductance fluctuations, LFN measurements were conducted. The observed $1/f$ noise behavior was consistent with the correlated mobility fluctuation (CMF) model across all oxygen pressure conditions. With increasing oxygen pressure, the extracted effective trap density (N_{it}) increased significantly from 0.74×10^{12} $eV^{-1}cm^{-2}$ to 6.77×10^{13} $eV^{-1}cm^{-2}$, surpassing the surface/interface trap density (N_{SS}) and dominating the charge transport mechanism. These results also clearly demonstrate that higher oxygen pressure shifts the dominant noise source from the ISO/dielectric interface to the main of the ISO channel, where fully oxidized indium atoms act as scattering centers, hindering carrier transport. This study highlights oxygen pressure's critical role in balancing AOS TFT electrical properties and defects, using LFN to explore transport mechanisms. These findings enhance understanding of V_O-induced instabilities and offer strategies to optimize AOS materials for future electronics.

2. Results and Discussion

To understand the influence of oxygen partial pressure on the electrical performance of ISO TFTs, devices were fabricated with a bottom-gate, top-contact configuration. **Figure 1**a illustrates the fabrication process flow and the corresponding device structure with the circuit overload. A 10-nm-thick ISO channel layer was deposited using DC magnetron sputtering, with systematic adjustment of the oxygen partial pressure. A two-step thermal annealing process was employed to improve interface properties and regulate oxygen vacancies. Figure 1b presents an optical micrography of the fabricated TFT with a typical channel length (L_{ch}) of 50 μm and width (W_{ch}) of 1000 μm. Other device configurations of the plane view of the device patterns are shown in **Figure S1** (see the

Supporting Information). To ensure result reproducibility, electrical measurements were performed in air on over 40 ISO TFTs for each oxygen-pressure condition. Figure 1c displays the transfer characteristics ($I_{ds}-V_{gs}$) of the ISO TFT under an Ar:O_2 partial pressure ratio of 11:1 at different V_{ds} values. The device exhibits typical n-type conduction with a current modulation ratio of approximately 10^7 at V_{ds}= 0.5 V. In addition, the transfer curves show a clockwise direction with nearly hysteresis-free operation, indicative of excellent gate controllability as well as low trapping densities at the ISO/dielectric interface. Direct evidence will be given and discussed later. Figure 1d illustrates the corresponding output characteristics ($I_{ds}-V_{ds}$) for the same TFT. The drain current I_{ds} in all curves increase linearly with V_{ds}, implying the formation of Ohmic contacts between the ISO channel and Mo electrodes. Further evidence of Ohmic contacts is provided by the transfer line method, as shown in **Figure S2**.

The impact of oxygen partial pressure during deposition on the fundamental properties of ISO TFTs is demonstrated by the transfer and output characteristics in Figures 1e and 1f, respectively. The semiconductor behavior of all the ISO films is retained, even at higher O_2 partial pressures. As the O_2 ratio increases, the V_{th} gradually shifts closer to V_{bg}= 0 V, and a pronounced hysteresis loop forms between the forward and reverse gate sweeps. The positive V_{th} shift is commonly attributed to the V_O reduction in an oxide-based semiconductor film,[37] while the presence of ΔV_{bg} suggests negative charges trapping at the channel/dielectric interface or injection into the dielectric from the active layer, which is a dynamic process for carrier capture/release.[38, 39] In addition, the slope of transfer curves from the off-state to the on-state significantly diminishes, along with a reduction in the I_{on}/I_{off} ratio. The output characteristics at V_{bg}= 40 V further confirm a reduction in I_{ds} with increasing oxygen partial pressure, as shown in Figure 1f. As is well-established, the existence of V_O serves as the primary contributor to charge transport

in AOSs by increasing free electron density. These observations strongly suggest that the variation of O_2 partial pressure leads to the modulation of device mobility and long-term operational stability.

For evaluating the uniformity of the ISO TFTs, static device parameters (e.g., V_{th}, ΔV_{bg}, I_{on}/I_{off}, μ, SS and N_{SS}) are statistically analyzed to assess the V_O contribution to the ISO TFTs under different deposition conditions, as illustrated in **Figure 2**a—2f. As shown in Figure 2a, the V_{th} shifts from —4.8 V to —2.3 V with the increase of oxygen concentrations, which can be attributed to the reduction of oxygen vacancy defect in the conducting channel. This reduction in oxygen vacancy defects is accompanied by a decrease in electron density, further supporting the relationship between oxygen concentration and dynamic carrier modulations. Figure 2b shows that the ΔV_{bg}, defined as the maximum of the difference during the transfer curve sweeping, increases to 5.1 V under the Ar:O_2 partial pressure ratio of 6:6 at V_{ds}= 0.5 V. This result suggests that higher oxygen concentrations enhance carrier trapping, leading to temporary charge capture and release in the ISO TFTs, which ultimately degrades device performance. The current modulation follows a similar trend, as shown in Figure 2c. These statistical findings strongly support the observations in Figure 1, again. Notably, as the O_2 partial pressure increases, the corresponding error bars expand significantly, indicating pronounced current fluctuations under a given electric field, likely caused by enhanced trapping/de-trapping effects and/or charge scattering events.

According to the conventional equation $\mu=\left(\frac{L_{ch}}{W_{ch}}\right)\cdot\left(\frac{d}{\varepsilon_0\varepsilon_r V_{ds}}\right)\cdot g_m$, where ε_0 is the permittivity in a vacuum, ε_r is 3.9 for SiO_2, d is the thickness of the dielectric layer, and $g_m=\frac{dI_{ds}}{dV_{bg}}$ is the transconductance.[34] The mobility, μ, can be estimated and presented

in Figure 2d as a function of the O_2 partial pressure ratio. Under the Ar:O_2= 11:1 deposition condition, the average mobility is 8.39 $cm^2V^{-1}sec^{-1}$ with a minor deviation of 2 %, which closely aligns with previous reports.[24] With the rise of the O_2 pressure, the μ value obviously drops by up to 20 % and expands its variation. The SS defined by $\frac{\partial V_{bg}}{\partial(\log I_{ds})}$ of the ISO TFTs was evaluated,[39] with the results shown in Figure 2e to assess interface defects between the ISO channel and the underlying substrate. The surface/interface trap density $N_{SS} = \left(\frac{\varepsilon_0 \varepsilon_r}{dq}\right)\left[\left(\frac{SS}{\ln(10)\cdot\frac{k_B T}{q}}\right) - 1\right]$ was further derived from the SS values and given in Figure 2f, where q, k_B, and T are the elementary charge, Boltzmann constant and absolute temperature in Kelvin, respectively.[39] It can be observed that increasing N_{SS} leads to enhanced charge trapping, which in turn raises SS. At a partial pressure ratio of 6:6, the averaged SS and N_{SS} values (0.82 V/decade and 1.24 $\times 10^{12}$ $eV^{-1}cm^{-2}$, respectively) are markedly much higher than other deposition conditions. In general, N_{SS} in AOS TFTs can be either due to defects at the dielectric surface, such as oxide dangling bonds, or channel imperfections, such as V_O, which are typically the dominant contribution in devices with non-optimized channels. SS and N_{SS} can provide a static estimation of the trap density but fail to differentiate between shallow and deep traps due to the limitations of DC measurements in capturing dynamic defect behaviors. Moreover, static characteristics often depend on data scanning rate and environmental factors, reducing the reliability of extracted parameters in defect quality assessment. An advanced strategy is essential to gain better insight into the effects of defect states on device performance, overcoming the limitations of DC measurements.

To comprehend additional optimization constraints for device performance and the

mechanism of underlying dynamic fluctuations, we preset the power spectral densities (PSDs) of current fluctuations, S_I, as a function of frequency with different applied V_{ds} and V_{bg} in **Figures 3**a and 3b for the Ar:O_2= 11:1 deposition condition. The S_I values increase with I_{ds}, correlating with increasing V_{ds} or V_{bg}, and consistently obey a classical 1/*f* dependence with a slope of ~1, suggesting the existence of a uniform distribution of defect states in space and energy in the ISO TFTs. A dashed line representing ideal 1/*f* dependence is included for comparison. The same 1/*f* dependence of the PSDs was observed under other deposition conditions (see **Figure S3** and **Figure S4** in the Supporting Information). Notice that no random telegraph signals have been detected, which also strongly supports the 1/*f* observations, as shown in **Figure S5-7**. Initially, the PSD of all the ISO TFTs under varying oxygen pressure conditions was characterized empirically using the formula, $S_I \propto I_{ds}^{\alpha} / f$ where α is the scaling exponent with the current. Figure 3c shows the PSDs as a function of I_{ds} at V_{bg}= 0 V for three different flow ratios (Ar:O_2= 11:1, 8:4, and 6:6) during film depositions. The PSD exhibits a quadratic increase across different V_{ds} values. The increase in I_{ds} does not induce fluctuations but rather enhances their visibility. The quadratic dependence on I_{ds} rules out current-induced heating effects, indicating that 1/*f* noise primarily arises from intrinsic resistor fluctuations. Consequently, the normalized PSDs (i.e., S_I / I_{ds}^2) at varying V_{ds} values can be further analyzed and are presented in Figure 3d. The normalized PSDs exhibit no dependence on V_{ds}, indicating that charge fluctuations likely originate from the ISO channel and/or the ISO/dielectric interface rather than the channel/contact barrier, highly consistent with transfer-line-method analysis.

Two predominant models describe the 1/*f* noise characteristics in conventional field-effect transistors: the charge number fluctuation (CNF) model and the Hooge mobility

fluctuation (HMF) model. The CNF model attributes noise generation to carrier trapping and de-trapping events occurring across a broad range of time constants at the dielectric/channel interface. These processes modulate the flat-band voltage, inducing fluctuations in charge carrier density. Under the assumption of a uniform trap distribution in energy and space, the PSD in the CNF model follows the relation of $\frac{S_I}{I_{ds}^2}=S_{Vfb}\cdot\left(\frac{g_m}{I_{ds}}\right)^2\propto\frac{1}{\left(V_{bg}-V_{th}\right)^2}$, where $S_{Vfb}=\frac{q^2k_BTN_{it}}{fW_{ch}L_{ch}}\cdot\left(\frac{d}{\varepsilon_0\varepsilon_r}\right)^2$ denotes the flat-band voltage spectral density.[40] In contrast, the HMF model attributes LFN to mobility fluctuations induced by variations in the lattice scattering cross-section, which alter the carrier collision probability in a homogeneous bulk. Within this framework, the normalized PSD is given by $\frac{S_I}{I_{ds}^2}=\frac{q\alpha_H\mu_{ds}}{L_{ch}^2f}\cdot\frac{1}{I_{ds}}\propto\frac{1}{\left(V_{bg}-V_{th}\right)}$ where α_H denotes the empirical Hooge parameter.[40] The dominant $1/f$ noise mechanism can be determined by analyzing the normalized PSDs as a function of $\left(V_{bg}-V_{th}\right)$ in a double-logarithmic plot. If the $\frac{S_I}{I_{ds}^2}$ scales with a power of -2, the noise is predominantly governed by the CNF model. Conversely, if it varies linearly with $\left(V_{bg}-V_{th}\right)$across weak to strong inversion, the HMF model is more applicable.

Figure 3e presents the normalized PSDs at f= 20 Hz for three different flow ratios with respect to $\left(V_{bg}-V_{th}\right)$. At lower O_2 partial pressure, the $\frac{S_I}{I_{ds}^2}$ tends to follow a slope of -2, which gradually shifts toward -1 as the oxygen concentration increases. Compared to bulk-scale devices, PSD analysis in nanoscale channels is more complex due to their pronounced environmental sensitivity. As a result, single-noise models often deviate significantly from experimental data. Due to the slope variation between -2 and

−1 (see Figure 3e), a combined model, so-called carrier number fluctuation−correlated mobility fluctuation (CMF), can be further considered. The CMF model links noise to fluctuations in interface trap occupancy, which correlates with carrier number variations and surface mobility. The combined model is expressed by $\frac{S_I}{I_{ds}^2}=S_{Vfb}\cdot\left(1+\frac{\alpha_{sc}\mu\cdot I_{ds}}{g_m}\cdot\frac{d}{\varepsilon_0\varepsilon_r}\right)\cdot\left(\frac{g_m}{I_{ds}}\right)^2$, where α_{sc} denotes the interfacial Coulomb scattering parameter.[39] Unlike the CNF model, the CMF model incorporates an additional Coulomb scattering term, originating from the electrostatic field of channel traps and appearing in the second term. Figure 3f plots the normalized PSDs versus I_{ds} at 20 Hz and V_{ds} = 0.1 V for three O_2 flow ratios, illustrating the dominant noise source. The solid lines depict the best fit of the CMF model across all ISO films, suggesting that V_O contributions during deposition cannot be explained by only a single transport factor in the AOSs. At higher oxygen partial pressures, mobility scattering from the channel becomes significant. The trends of both CNF and HMF models are included as visual references.

With the variation of the O_2 partial pressure, the α_{sc} values can be further analyzed based on the CMF model, as shown in **Figure 4**a. As the oxygen centration increases during the film deposition, the α_{sc} rises significantly from 0.67×10^5 V sec C^{-1} at Ar:O_2= 11:1 to 3.22×10^5 V sec C^{-1} at 6:6. This indicates that bulk effects (i.e., channel scattering centers) play a dominant role in charge transport and dynamic noise. The N_{it}, which provides insights into total charge trapping in devices, can be calculated and compared with the N_{SS} as shown in Figure 4b. At the 11:1 condition, the N_{it} of 0.74×10^{12} $eV^{-1}cm^{-2}$, comparable to the N_{SS} of 0.65×10^{12} $eV^{-1}cm^{-2}$, suggests that the same trapping states contribute to both quasistatic and dynamic noise measurements. This implies that noise fluctuations primarily originate from the ISO/dielectric interface. As oxygen

concentrations increase, the N_{it} rises to 6.77×10^{13} $eV^{-1}cm^{-2}$, an order of magnitude higher than the N_{SS} of 1.23×10^{12} $eV^{-1}cm^{-2}$. This indicates that the primary source of charge noise gradually shifts from the ISO/dielectric interface to the ISO channel. This further confirms that with increasing oxygen partial pressure, carrier transport in the conducting channel is increasingly governed by scattering mechanisms, gradually replacing charge trapping/de-trapping at the dielectric interface. Excessive carrier scattering in the channel ultimately reduces mobility and ON-current, degrading device performance. The N_{it} profiles were analyzed as a function of z/λ [42] and are presented in Figure 4c. Here, z represents the frequency dependence of the tunneling depth, while λ (10^{-8} cm for general transistors) is the tunneling distance parameter. As shown in Figure 4c, the N_{it} values are independent of z/λ across all conditions, demonstrating consistency with the observed $1/f$ behaviors. The lower N_{it} observed in the 11:1 condition suggests fewer scattering events, leading to improved device performance.

InO-based materials feature ionic bonds between indium *s* orbitals and oxygen 2*p* orbitals. The strong ionicity of InO-based materials drives charge transfer from indium to oxygen, elevating cation energy levels while lowering those of anions. As a result, the conduction band primarily comprises unoccupied indium *s* orbitals, while fully occupied oxygen 2*p* orbitals constitute the valence band. Indium atoms with dangling bonds, i.e., oxygen vacancies, introduce energy levels near the conduction band edge, functioning as shallow donors. Figure 4d schematically illustrates this concept: indium atoms with V_O act as conductors, supplying free carriers while simultaneously serving as charge-trapping defects (see Figure 4d(i)). Charge transport is primarily governed by the ISO/dielectric interface at a low O_2-ratio condition. With increasing O_2 ratio, fully oxidized indium atoms act as insulators and charge-scattering centers (see Figure 4d(ii)), degrading device performance. Controlling oxygen concentration during AOS film deposition is crucial for

regulating V_O formation as well as balancing interface and bulk effects.

Conclusion

This study demonstrates the critical influence of oxygen partial pressure on the electrical performance and charge transport mechanisms of ISO TFTs. By systematically tuning the Ar:O_2 ratio during film deposition, we identify a clear transition in transport behavior: at lower O_2 pressures, charge fluctuations are primarily governed by the interface, whereas at higher O_2 pressures, bulk scattering effects become dominant. The increase in SS, V_{th} variability, and mobility degradation at high O_2 pressures is attributed to enhanced charge trapping and scattering from fully oxidized indium atoms. LFN analysis further confirms this transition, revealing a shift from CNF to CMF models as the primary noise mechanism. These results underscore the importance of oxygen-pressure control in AOS film deposition, offering a strategic approach to optimize the trade-off between carrier transport efficiency and long-term stability. Our findings provide valuable insights into defect engineering for future high-performance oxide semiconductor devices, particularly in low-power and high-mobility applications.

Method

Device fabrications: Amorphous ISO TFTs were fabricated on heavily doped p-type silicon substrates featuring a 250 nm thermally grown SiO_2 layer. A 10-nm ISO semiconductor layer, doped with low SiO_2 concentrations (In_2O_3: SiO_2 = 90:10 by weight), was deposited using DC magnetron sputtering (Shibaura Mechatronics CFS-4EP-LL i-miller) to ensure environmentally stable operation.[28] Active channels (10-nm thick) were deposited at 0.25 Pa total pressure and 200 W sputtering power, using Ar:O_2 gas mixtures of 11:1, 8:4, and 6:6. After deposition, the ISO thin films were thermally annealed at 250 ℃ for 30 minutes in ambient air. Electron-beam evaporation was used to deposit 40-nm molybdenum (Mo) through a stencil shadow mask, forming channels with lengths of 50–350 μm and a fixed width of 50 μm. The devices were annealed again at 150 ℃ for 30 minutes in ambient air. The devices used in this work have a simple inverted staggered configuration without additional passivation on top of the ISO conducting channels. Further fabrication details are available in the previous report.[24]

Device characterizations: Optical images of device configurations were captured using an Olympus BX53 optical microscope. Electrical characterizations of ISO TFTs were performed at room temperature in ambient conditions using a Lakeshore TTPX probe station coupled with a Keysight B2912A dual ─ channel source/measure unit. To minimize environmental fluctuations, all measurements were conducted in a dark chamber. Low-frequency noise properties of ISO TFTs were examined using a programmable point-probe noise measurement system (3PNMS, Synergy Concept) over a frequency range of 1 Hz to 1 kHz to elucidate dynamic charge transport mechanisms. Throughout the experiments, all devices were fully grounded. The background noise floor was 2×10^{-27} A^2 Hz^{-1}.

Supporting Information

Supporting Information is available from the Wiley Online Library or from the author.

Acknowledgements: This research was supported by the National Science and Technology Council, Taiwan (NSTC 112-2628-M-005-001-MY3, 113-2119-M-007-015-MBK, 113-2811-M-005-020, and 113-2811-M-005-024). All authors thank Prof. Aikawa Shinya (Kogakuin University, Japan) for useful discussion on film fabrication. We also deeply thank Jie Dong Co. for facility support.

Author contributions

C.-Y.L., P.-W.C, K.T., and Y.-F.L. designed the experiments. Y.-C.K. and Y.-C.L. contributed equally to this work. K.T. synthesized and characterized materials and fabricated the devices. Y.-C.L., F.-S.Y., Y.-M.C., and C.-Y.L. carried out the electrical characterizations. C.-Y.L., Y.-C.L., and Y.-F.L. analyzed the experimental data and prepared the figures. Y.-C.K., C.-Y.L., and Y.-F.L. wrote the manuscript. All authors participated in the discussion of the results and revision of the manuscript and commented on the manuscript.

References

[1] A. Janotti, C. G. Van de Walle, *Appl. Phys. Lett.* **2005**, 87, 122102.

[2] D. C. Look, G. C. Farlow, P. Reunchan, S. Limpijumnong, S. B. Zhang, K. Nordlund, *Phys. Rev. Lett.* **2005**, 95, 225502.

[3] B. Matthias, D. Ulrike, *Prog. Surf. Sci.* **2005**, 79 47.

[4] T. Kamiya, H. Hosono, *NPG Asia Mater.* **2010**, 2, 15.

[5] F. Wang, C. D. Valentin, G. Pacchioni, *Phys. Rev. B* **2011**, 84, 073103.

[6] H. K. Noh, K. J. Chang, B. R. Ryu, W. J. Lee, *Phys. Rev. B* **2011**, 84, 115205.

[7] J. S. Park, W. J. Maeng, H. S. Kim, J. S. Park, *Thin Solid Films* **2012**, 520, 1679.

[8] J. Wang, R. Chen, L. Xian, S. Komarneni, *Ceram. Int.* **2018**, 44, 7357.

[9] D. Guo, Q. Guo, Z. Chen, Z. Wu, P. Li, W. Tang, *Mater. Today Phys.* **2019**, 11, 100157.

[10] K. Ide, K. Nomura, H. Hosono, T. Kamiya, *Phys. Status Solidi A* **2019**, 216, 1800372.

[11] Q. H. Li, Y. X. Liang, Q. Wan, T. H. Wang, *Appl. Phys. Lett*. **2004**, 85, 6389.

[12] S. Song, W. K. Hong, S. S. Kwon, T. Lee, *Appl. Phys. Lett*. **2008**, 92, 26.

[13] K. Ide, Y. Kikuchi, K. Nomura, M. Kimura, T. Kamiya, H. Hosono, *Appl. Phys. Lett*. **2011**, 99, 093507.

[14] J. Yao, N. Xu, S. Deng, J. Chen, J. She, H. P. David Shieh, P. T. Liu, Y. P. Huang, *IEEE Trans. Electron Devices* **2011**, 58, 1121.

[15] A. Charnas, Z. Zhang, Z. Lin, D. Zheng, J. Zhang, M. Si, P. D. Ye, *Adv. Mater.* **2024**, 36, 2304044.

[16] Y. C. Chang, S. T. Wang, Y. T. Lee, C. S. Huang, C. H. Hsu, T. T. Weng, C. C. Huang, C. W. Chen, T. T. Chou, C. Y. Chang, W. Y. Woon, C. L. Lin, J. Y. C. Sun, D. H. Lien, *Adv. Mater.* **2024**, doi.org/10.1002/adma.202413212.

[17] J. Y. Kwon, D. J. Lee, K. B. Kim, *Electron. Mater. Lett.* **2011**, 7, 1.

[18] A. Suresh, J. F. Muth, *Appl. Phys. Lett*. **2008**, 92, 033502.

[19] K. Nomura, T. Kamiya, H. Hosono, *J. Inf. Disp.* **2010**, 18, 789.

[20] P. Migliorato, M. D. H. Chowdhury, J. G. Um, M. Seok, J. Jang, *Appl. Phys. Lett*. **2012**, 101, 123502.

[21] Y. S. Shiah, K. Sim, Y. Shi, K. Abe, S. Ueda, M. Sasase, J. Kim, H. Hosono, *Nat. Electron.* **2021**, 4, 800.

[22] S. Aikawa, P. Darmawan, K. Yanagisawa, T. Nabatame, Y. Abe, K. Tsukagoshi, *Appl. Phys. Lett*. **2013**, 102, 102101.

[23] S. Aikawa, T. Nabatame, K. Tsukagoshi, *Appl. Phys. Lett*. **2013**, 103, 172105.

[24] N. Mitoma, S. Aikawa, X. Gao, T. Kizu, M. Shimizu, M. F. Lin, T. Nabatame, K. Tsukagishi, *Appl. Phys. Lett*. **2014**, 104, 102103.

[25] T. Kizu, S. Aikawa, N. Mitoma, M. Shimizu, X. Gao, M. F. Lin, T. Nabatame, K. Tsukagishi, *Appl. Phys. Lett*. **2014**, 104, 152103.

[26] W. Ou-Yang, N. Mitoma, T. Kizu, X. Gao, M. F. Lin, T. Nabatame, K. Tsukagishi, *Appl. Phys. Lett*. **2014**, 105, 163503.

[27] N. Mitoma, S. Aikawa, W. Ou-Yang, X. Gao, T. Kizu, M. F. Lin, A. Fujiwara, T. Nabatame, K. Tsukagishi, *Appl. Phys. Lett*. **2015**, 106, 042106.

[28] S. Aikawa, N. Mitoma, T. Kizu, T. Nabatame, K. Tsukagishi, *Appl. Phys. Lett*. **2015**, 106, 192103.

[29] W. Song, L. Lan, P. Xiao, Z. Lin, S. Sun, Y. Li, *IEEE Trans. Electron Devices* **2016**, 63, 4315.

[30] K. A. Stewart, V. Goulioukˇ, D. A. Keszler, J. F. Wager, *Solid-State Electron.* **2017**, 137, 80.

[31] A. A. Balandin, *Nat. Nanotechnol.* **2013**, 8, 549.

[32] J. M. Lee, W. S. Cheong, C. S. Hwang, I. T. Cho, H. I. Kwon, J. H. Lee, *IEEE Electron Device Lett.* **2009**, 30, 505.

[33] N. Clement, K. Nishiguchi, A. Fujiwara, D. Vuillaume, *Nat. Commun.* **2010**, 1, 92.

[34] Y. F. Lin, Y. Xu, C. Y. Lin, Y. W. Suen, M. Yamamoto, S. Nakaharai, K. Ueno, K. Tsukagoshi, *Adv. Mater.* **2015**, 27, 6612.

[35] L. Anh T. Nguyen, J. Jiang, T. D. Nguyen, P. Kim, M. K. Joo, D. L. Duong, Y. H. Lee, *Nat. Electron.* **2023**, 6, 582.

[36] W. Shin, J. Y. Lee, R. H. Koo, J. Kim, J. H. Lee, S. Y. Lee, S. T. Lee, *Adv. Electron. Mater.* **2024**, 10, 2300515.

[37] K. H. Ji, J. I. Kim, H. Y. Jung, S. Y. Park, R. Choi, U. K. Kim, C. S. Hwang, D. Lee, H. Hwang, J. K. Jeong, *Appl. Phys. Lett*. **2011**, 98, 103509.

[38] M. Kimura, T. Nakanishi, K. Nomura, T. Kamiya, H. Hosono, *Appl. Phys. Lett*. **2008**, 92, 133512.

[39] D. K. Schroder, Semiconductor Material and Device Characterization, 3rd ed., John Wiley & Sons, Hoboken, NJ, USA **2006**.

[40] G. Ghibaudo, O. Roux, C. Nguyen-Duc, F. Balestra, J. Brini, *Phys. Status Solidi* **1991**, 124, 571.

[41] F. N. Hooge, *IEEE Trans. Electron Devices* **1994**, 41, 1926.

[42] M. V. Haartman, M. Ostling, *Low-frequency Noise in Advanced MOS devices*, 1st ed.; Springer Publishing Company, Incorporated **2007**.

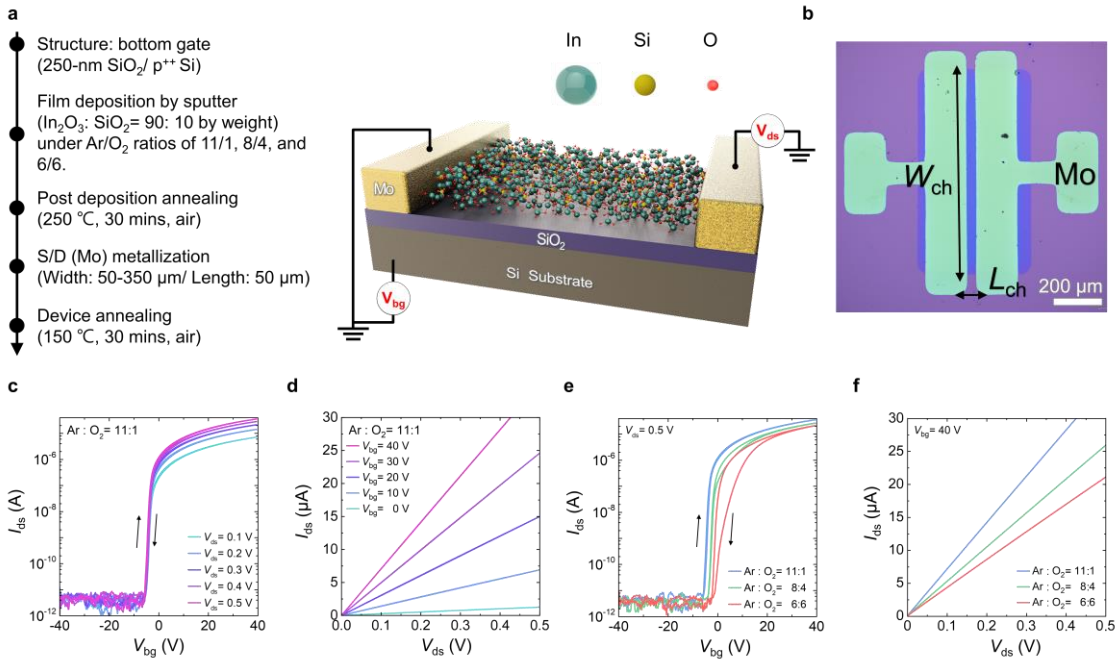

Figure 1. (a) Fabrication process flow of a bottom-gate ISO TFT and its corresponding device structure with the circuit overload. The p^{++}-Si substrate and 250-nm thick SiO_2 act as a back-gate electrode and dielectric, respectively. Mo deposited through a stencil shallow mask are used as source (S)/drain (D) electrodes. (c) Optical image of a fabricated ISO TFT with W_{ch} /L_{ch}= 1000 μm/50 μm. (d) Transfer characteristics of an ISO TFT at different V_{ds} from 0.1 to 0.5 V. (e) The corresponding output characteristics at different V_{gs} from 0 to 40 V. The oxygen partial pressure during film deposition is set as Ar:O_2= 11: 1. (f) Transfer and (g) output characteristics of the ISO TFTs under three different flow ratios (Ar:O_2= 11:1, 8:4 and 6:6) for film depositions.

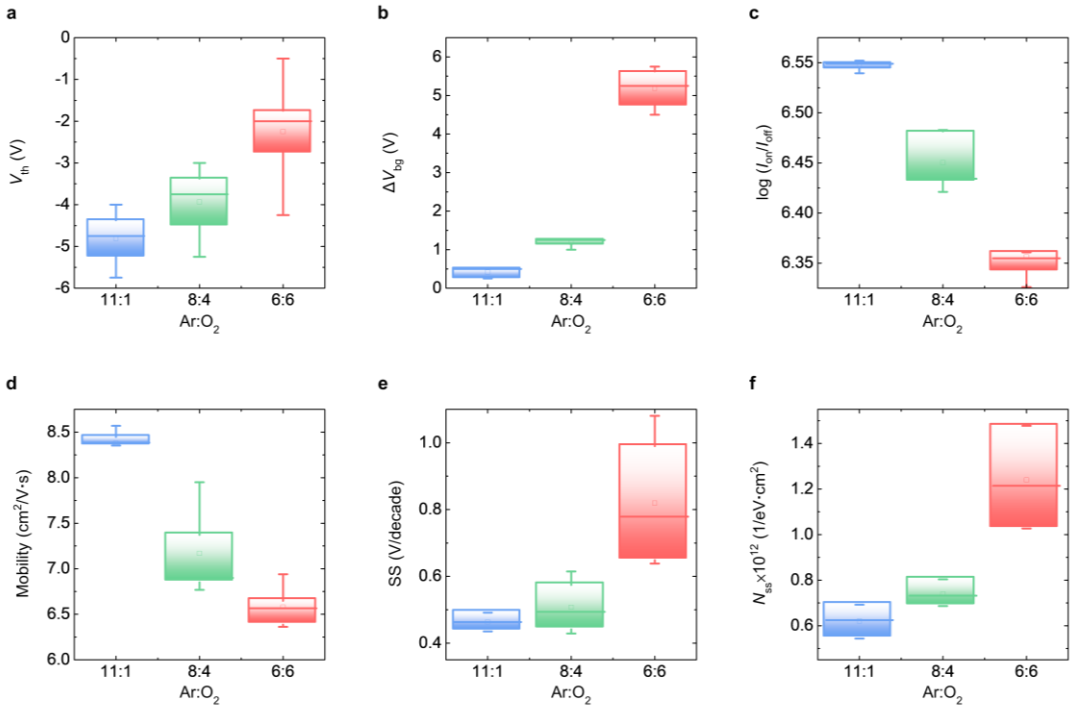

Figure 2. Statistical results for (a) V_{th}, (b) ΔV_{bg}, (c) I_{on}/I_{off} current modulation, (d) mobility, (e) *SS*, and (f) N_{SS} derived from the transfer characteristics of ISO TFTs grown under different deposition conditions (Ar:O_2= 11:1, 8:4 and 6:6).

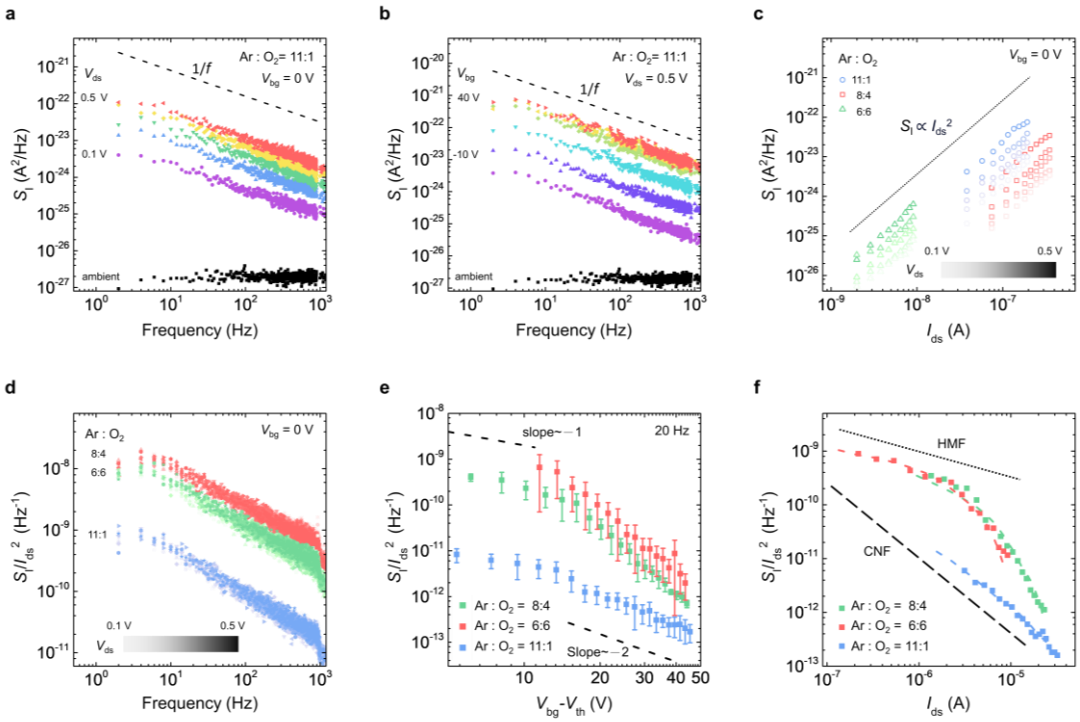

Figure 3. PSDs of the current fluctuations S_I as a function of frequency at room temperature for an ISO TFT under Ar:O_2= 11:1 flow ratio at (a) different V_{ds} and (b) different V_{bg}. Dashed lines denote the ideal 1/*f* dependence. Frequency-independent background noise floor is shown here. (c) S_I as a function of I_{ds} at different V_{ds} for the ISO TFTs grown under three different deposition conditions (Ar:O_2= 11:1, 8:4, and 6:6). Dotted line denotes the $S_I \propto I_{ds}^2$ relationship. S_I normalized by the square of I_{ds} (d) as a function of frequency at different V_{ds}, (e) as a function of ($V_{bg} - V_{th}$), and (f) as a function of I_{ds} for the ISO TFTs grown under three different flow ratios (Ar:O_2= 11: 1, 8: 4 and 6: 6) for film depositions. Solid lines in (f) denote the best-fit results.

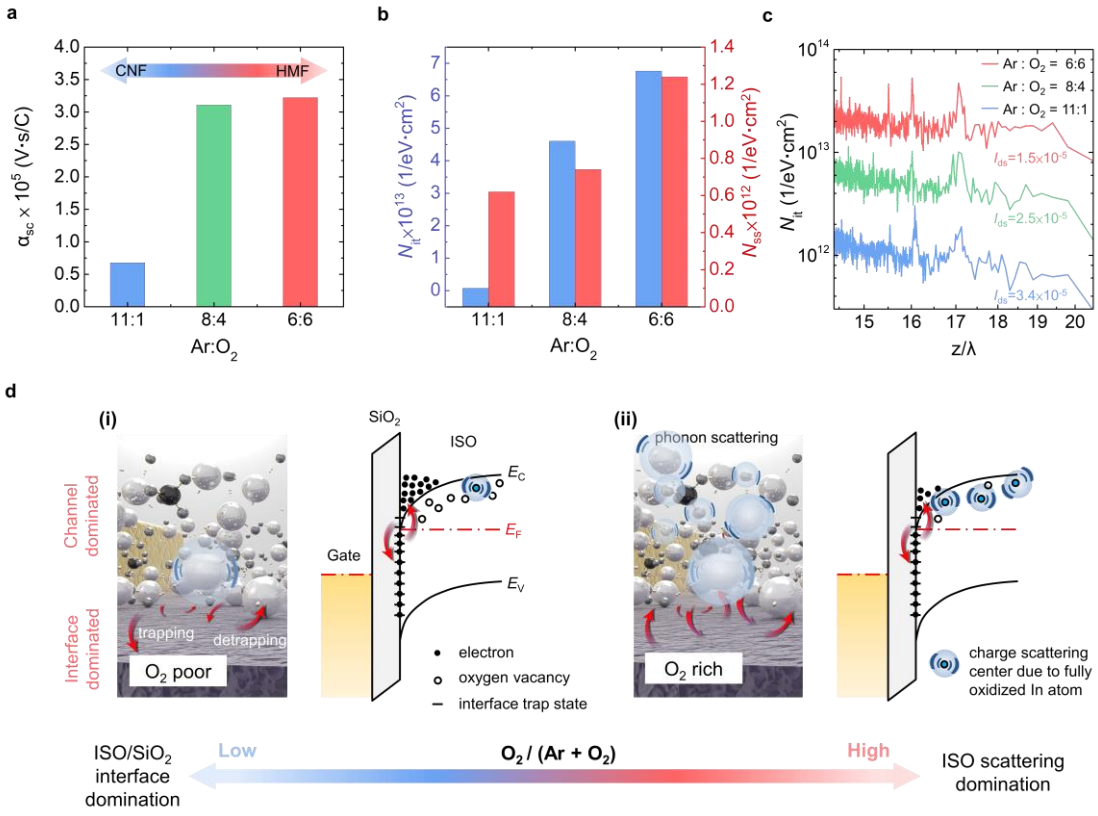

Figure 4. (a). Extracted α values and (b) N_{it} for three different O_2 flow conditions. (c) Extracted N_{it} depending on z/λ for three flow conditions, where z and λ represent the trap depth and the tunneling distance parameter, respectively. (d) Schematic illustrations and the corresponding band diagrams under (i) low and (ii) high O_2 partial pressure for film depositions.

The table of contents entry should be 50−60 words long, and the first phrase should be bold. The entry should be written in the present tense and impersonal style.

Oxygen Pressure Control steers charge transport from interface charge trapping to bulk scattering in silicon-doped In_2O_3 thin-film transistors. Low-frequency noise analysis reveals that, with increasing O_2 partial pressure, fully oxidized indium atoms become active scattering centers. This study demonstrates an oxygen-engineering strategy to optimize device performance and stability.

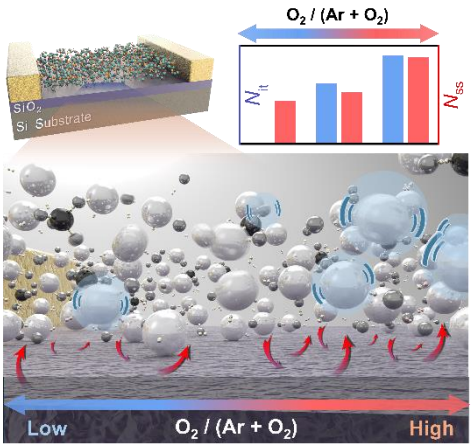

Keywords: metal oxide semiconductor, thin-film transistors, Low-frequency noise, oxygen pressure, charge transport mechanism